

# Cryogenic focal plane flatness measurement with optical zone slope tracking

Jerry Edelstein<sup>1</sup>, Martin Sirk<sup>1</sup>, Patrick N. Jelinsky<sup>1</sup>, Robert W. Besuner<sup>1</sup>, Matthew Hoff<sup>2</sup>, Paul Perry<sup>2</sup>, Henry D. Heetderks<sup>1</sup>, Christopher J. Bebek<sup>2</sup>, Michael E. Levi<sup>2</sup>

<sup>1</sup> U.C. Berkeley Space Sciences Laboratory

<sup>2</sup> Lawrence Berkeley National Laboratory

## ABSTRACT

We describe a non-contact optical measurement method used to determine the surface flatness of a cryogenic sensor array developed for the JDEM mission. Large focal planes envisioned for future visible to near infra-red astronomical large area point-source surveys such as JDEM, WFIRST, or EUCLID must operate at cryogenic temperatures while maintaining focal plane flatness within a few 10's of  $\mu\text{m}$  over half-meter scales. These constraints are imposed by sensitivity conditions that demand low noise observations from the sensors and the large-field, fast optical telescopes necessary to obtain the science yield. Verifying cryogenic focal plane flatness is challenging because  $\mu\text{m}$  level excursions need to be measured within and across many multi-cm sized sensors using no physical contact and while situated within a high-vacuum chamber. We have used an optical metrology Shack-Hartmann scheme to measure the 36x18 cm focal plane developed for the JDEM mission at the Lawrence Berkeley National Laboratory. The focal plane holds a 4x8 array of CCDs and HgCdTe detectors. The flatness measurement scheme uses a telescope-fed micro-lens array that samples the focal plane to determine slope changes of individual sensor zones.

**Keywords:** Flatness, metrology, JDEM, WFIRST, CCD, HgCdTe, Silicon Carbide, Space Telescope

## 1 INTRODUCTION

Large focal planes envisioned for future visible to near infra-red astronomical large area surveys such as JDEM, WFIRST, or EUCLID must operate at cryogenic temperatures while maintaining focal plane flatness within a few 10's of  $\mu\text{m}$  over half-meter scales. These constraints are imposed by sensitivity conditions that demand low noise observations from the sensors and the large-field, fast optical telescopes necessary to obtain the science yield.

We have developed an optical surface profilometer in order to verify the cryogenic flatness of a focal plane that contains a mixed array of 32 CCD and HgCdTe detectors mounted on a SiC structure and covering a 36x18 cm active area. The focal plane was developed<sup>1</sup> at the Lawrence Berkeley National Laboratory as a technology demonstrator for the JDEM mission. The cryogenic flatness of the Demonstrator constitutes important metrology verification for ultimate mission science performance based on requirements established for the former proposed SuperNova/Acceleration Probe<sup>2</sup> (SNAP) and JDEM space telescopes. Some of the key mechanical and thermal performance goals include detector focal surface flatness better than 40  $\mu\text{m}$  P-V cold across 36 cm, at operating at temperatures as low as 120K.

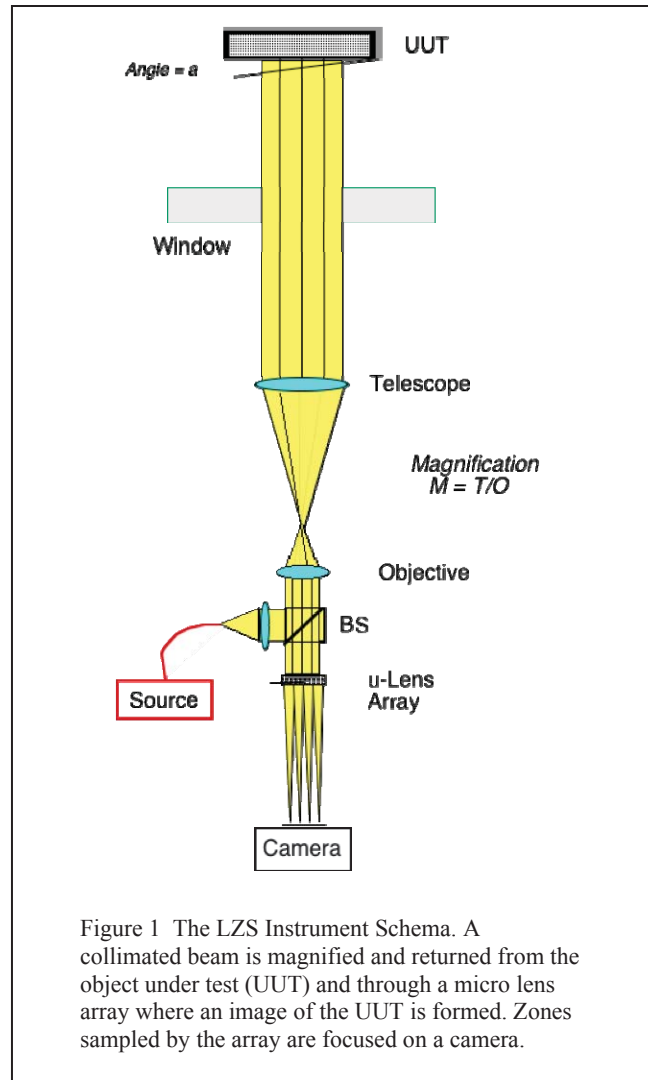
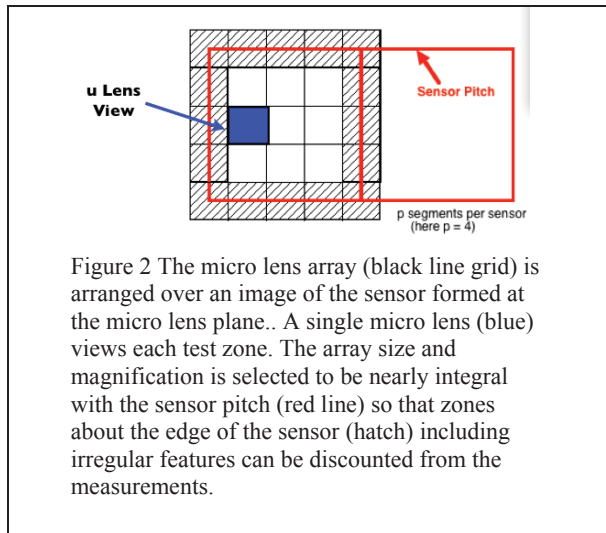
Verifying cryogenic focal plane flatness is challenging because excursions of a few  $\mu\text{m}$  need to be measured without physical contact both across half-meter scales and within numerous multi-cm sized sensors - all operating from room to cryogenic temperatures within a vacuum vessel. Our objective was to provide validation data on the mode and magnitude of numeric thermo-mechanical distortion models of the focal plane and sensors. We planned to first perform non-contact optical metrology over the focal plane at room temperature with a coordinate measuring machine and then to examine changes over the sensors and focal plane as a result of cooling. To accomplish this, we chose a measurement scheme that observes the change in slope of numerous individual regions over each sensor within a large fraction of the focal plane. The results have revealed useful information regarding the surface form of CCD and NIR detector packages as well as the entire focal plane.

## 2 SURFACE MEASUREMENT

We considered a number of possible schemes for non-contact surface measurement of the change in surface profile from room to cryogenic temperature. We considered methods to either directly measure the surface coordinates or, alternatively, to measure changes in the slope of the surface - from which the surface topology can be derived. The key measurement requirements are to measure a flatness deviation of up to 50  $\mu\text{m}$  with a precision of at least 5  $\mu\text{m}$  over a 36 cm x 10 cm region, presuming a local surface slope no greater than 5  $\mu\text{m}/\text{cm}$ . We sought a measurement method that would require a minimum of modifications to the available JDEM cryo-vacuum testing chamber facility and that would not challenge its pristine high-vacuum environment.

### 2.1 Measurement schemes

Laser displacement sensors products (e.g. by Keyence and Micro-Epsilon) can accurately measure surface height with respect to a reference flat. The devices use a linear array to sense changes in the reflected position of a returned laser beam launched at an acute angle. The displacement sensor measures a sub-mm sized region and must be translated in two dimensions over the test surface. While the units' several mm range and sub- $\mu\text{m}$  resolution are sufficient, they are not constructed for clean high-vacuum application and have maximum standoff distance of 5 to 15 cm. In our application, these limits would demand re-engineering the unit for clean vacuum operations, or the use of either a special vacuum chamber designed to include multiple viewports close to the focal plane face, or encasing the measurement unit within a windowed, atmospheric sub-chamber inside the vacuum test chamber. Placing large area viewports close to the focal plane would impose substantial thermal loading.



The DECAM<sup>3</sup> project measured a large CCD focal plane flatness through a dewar window using a commercial confocal chromatic displacement measurement system<sup>3</sup>. The surface location is determined at a single point by using the differential position of reflected colored light cones focused on the test object at different depths by a chromatic lens. The devices offer a range of standoff distance, resolution and accuracy, and can be made vacuum compatible. In our application, standoff distance limits would again require either a multi-windowed vacuum chamber door close to the focal plane face, or constructing a precision 2-dimensional motion stage within the vacuum test chamber.

Classical interferometry can be used to measure surface topology with sub- $\mu\text{m}$  precision and, with phase tracking

techniques, can be used to measure over a substantial range. For this very sensitive method to succeed, however, the interferometer, vacuum test chamber, and test object must all be mechanically stable so that a clear fringe pattern can be obtained. We tested our vacuum test chamber stability with all vacuum systems disabled and found a positional jitter of  $\sim 1 \mu\text{m}$ , a level at which fringe recording would be degraded. This method is more sensitive than our application requires, so we choose a technique that does not require extensive vibration isolation.

## 2.2 Local zone slope surface measurement

We chose to develop a non-contact surface metrology scheme that simultaneously measures the change in slope of multiple contiguous, localized zones on the test surface. The change in surface topography is derived from this “local zone slope” (hereafter “LZS”) method by an interpolation and summation of the slope–distance product from zone to zone. Adding this change to a base-line profile measured by conventional coordinate machines yields the absolute surface profile. By measuring many zones across each sensor, deviations within the sensor themselves can be examined along with the overall deviation of the focal plane surface. The scheme is an application of Shack-Hartmann profilometry<sup>45</sup>

In brief, the LZS scheme measures the reflected angle of collimated light from focal-plane zones illuminated by a collimated source. Consequently, the LZS device can be located outside of the vacuum test chamber and view the test object through a single optical port using a fixed, collimated source at large (meter) standoff distances to the test the surface. The validity of the LZS approach requires that the object under test change slope gradually on the physical scale of measurement zones and gaps between the zones. Significant slope changes on such scales are essentially impossible for a high-stiffness, monolithic focal plane material such as the SiC used in the Demonstrator.

## 3 THE LZS INSTRUMENT

The LZS instrument is schematically illustrated in Figure 1. A collimated beam is produced via a fiber fed telescope with magnification ratio,  $M$ . The collimated beam is injected into the vacuum chamber through a plane window. The collimated beam reflects from the test object back through the telescope to a micro-lens array (MLA) of focal length,  $L$ , which is located at the image plane of the object (see Figure 2). Each micro-lens then samples returned light from a local region, or zone, and brings it to focus on a camera at a ‘foci measurement plane’. A local zone’s focal spot will translate by a displacement,  $d$ , on the sensor according to the zone’s angle,  $a$ , by  $d = 2 a M L$  (see Figure 3). Hence each zone’s slope can be independently measured. The surface height,  $z$ , is derived from the accumulated interpolation over  $i=1..N$  zones with surface slopes,  $m_i$ , over their spans,  $x_i$ , such that  $z = \sum_i(m_i x_i)$ . Both errors in determining a zone’s slope and its span must be controlled as they each influence the error in derivation of surface height,  $dz_i = m_i dx_i + x_i dm_i$ . The total error in determining the flatness will be,  $\Delta z = \sqrt{N} dz_i$ , if the zone errors are uncorrelated. The location of the zone to be measured on the sensor is arranged and inspected by focusing the camera on the MLA plane. The MLA is

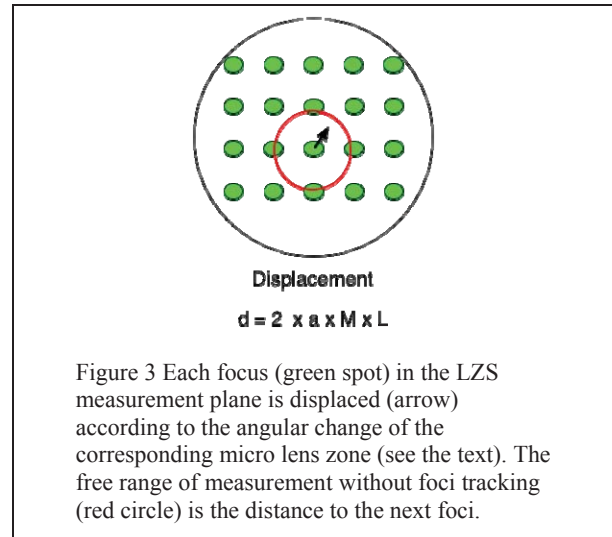


Figure 3 Each focus (green spot) in the LZS measurement plane is displaced (arrow) according to the angular change of the corresponding micro lens zone (see the text). The free range of measurement without foci tracking (red circle) is the distance to the next foci.

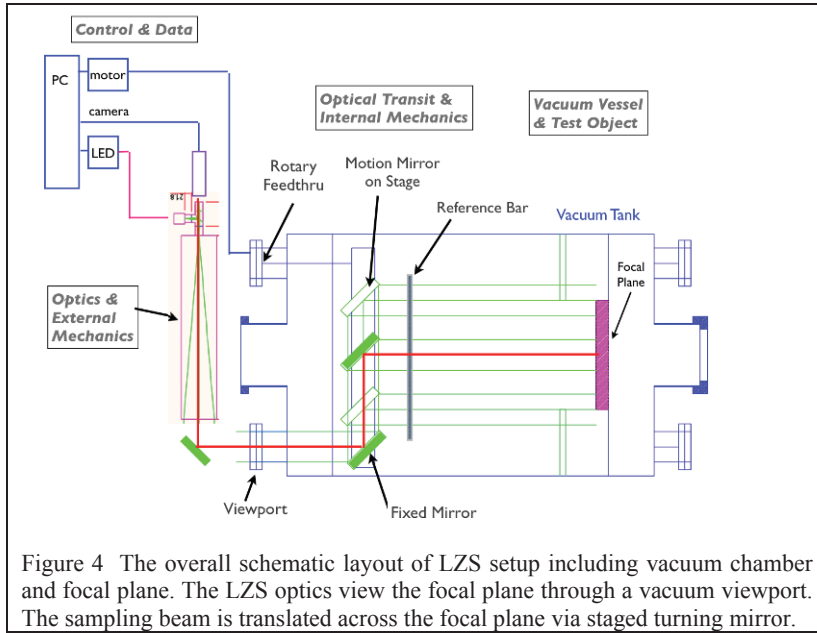
Table 1 LZS surface measurement requirements

Parameter	Requirements
Flatness Error	< 5 $\mu\text{m}$ over 36 x 12 cm.
Slope Range	< 5 $\mu\text{m} / \text{cm}$
Slope Accuracy	< 0.2 $\mu\text{m} / \text{cm}$
Sensor Pitch	4.5 cm
Zones Per Sensor	> 4
Positional Accuracy	< 0.1 mm

installed on staging that allows for lateral and rotational adjustment. In this way the sample zones can be placed within the sensor active area and avoid sensor boundaries where we anticipate significant non-uniformities can exist (see Figure 2). The image also establishes each zone’s absolute geometric position on the focal plane.

A number of LZS instrument parameters must be simultaneously considered as they affect the resolution and range of surface profile measurements. A change in surface slope in a zone results in a micro-lens focus transit on the detector and the slope sensitivity is proportional to

the collimator magnification and the micro lens focal length. The slope measurement resolution is then set by the detector's resolution and the quality of the MLA focal spot. The detector resolution should sufficiently sample the spot size for accurate centroiding. The measurement data consists of a grid of MLA foci spaced at the micro lens pitch. Without active foci tracking, the data interpretation may become confusing if the zone slope moves a focus by more than this pitch. Under this constraint, the slope measurement range becomes proportional to the micro lens pitch and inversely so to the slope sensitivity. The micro lens pitch and the collimator magnification also establish the number and size of zones per sensor (see Figure 2). Ideally the zones will sample the sensor pitch in integral units such that the sampling regions will be regular and well spaced across the several sensor units. The LZS resulting measurement requirements are summarized in Table I.



The overall layout of the LZS metrology system is illustrated in Figure 4. The LZS instrument is installed on the JDEM cryo-vacuum test chamber. An optical source and measurement sub-system is located outside of the vacuum test chamber and mounted to the chamber door (see Figure 5). An optical transit system that redirects the 10 cm tall sample beam over the focal plane is attached to the inside of a chamber door (see Figure 6). The focal plane under test is mounted at the opposite end of the vacuum chamber (see Figure 7).

The transit system is arranged at a 15-degree angle with respect to the focal plane height to increase the vertical coverage and aid detection of asymmetric distortions. The high-vacuum chamber facility is cryo and ion pumped and includes mounting hardware and feedthroughs for the Demonstrator focal plane<sup>6</sup>, electronic harnessing, liquid nitrogen, electrical heater control, and temperature monitors for thermal cycle control. The facility permits clean room environment handling and installation of the focal plane to the chamber.



Figure 5 The LZS instrument mounted to the JDEM vacuum test chamber door. The sample beam enters a viewport to the right.

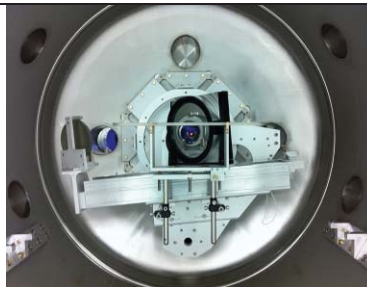


Figure 6 The optical transit system attached to the vacuum chamber door interior uses a stage mirror (at center) to move the sample beam over the focal plane. Illumination via the viewport is visible (red spot, center). Also visible is a thin reference mirror spanning the beam view path.



Figure 7 The Demonstrator focal plane mounted at the far end of the vacuum chamber. The transit mirror is visible on the tank door, left.

The detailed LZS instrumental arrangement and parameters for our implementation are summarized in Table 2 and are as follows. A sampling beam is generated using a source and a telescope. The source is a 635nm LED to avoid laser speckle or chromatic aberrations. The telescope consists of a 40 mm focal length objective and a 100 mm diameter, 600 mm focal length commercial telescope tube. The collimated beam is turned by a tip-tilt mounted elliptical flat mirror and enters the vacuum chamber via an AR coated fused silica viewport. A fixed elliptical flat mirror turns the beam toward a linear stage axis that parallels the focal plane face. The beam is turned toward the focal plane with a tip-tilt mounted 15 cm diameter flat mirror that rides on the linear stage. A 200 step per revolution motor drives the linear stage's 10-turn per cm lead screw via a sealed bellows, magnetically coupled rotary feed through. In this way the 10 cm tall sample beam can be accurately positioned across the full width of the focal plane. The turn mirrors' angles are adjusted so that the sample beam returns from the focal plane, about 1.35m from the telescope, through the telescope and to the MLA. An axial-staged CCD camera is focused on the MLA and used to make it coincident with the focal plane's image. The MLA is a rectangular filled 0.5 mm grid with 21.8 mm focal length. The camera is repositioned to coincide with the MLA focus for slope measurements. A gauge block is used for changing positions between image and measurement planes in order to maintain scale calibrations. The CCD camera has 1024 x 1280 pixels of 6.7 $\mu$ m size and uses a 1:1 telecentric image transfer lens with 40 mm focal length. The camera is operated overnight prior to measurements to thermally stabilize the pixel scale during measurements.

Table 2 LZS instrumental design parameters

LZS Design Parameters	
Collimator Aperture	10 cm
Collimator Magnification	15
MLA Focal Length	21.8 mm
MLA Cell Pitch	0.500 mm
Measurement Zone Size	7.3 mm
Detector Pixel Size	6.7 $\mu$ m
Detector Pixel Count	1024 x 1280
Pixels / MLA Diffraction Spot	7
Slope Sensitivity	0.13 $\mu$ m / cm
Slope Range	6 $\mu$ m / cm

## 4 LZS MEASUREMENTS

### 4.1 Alignment and Calibration

The LZS system alignment and calibration procedures were established by observing a 35 x 18 cm glass mirror located at the position of the focal plane. The calibration mirror was made flat to  $< \lambda/4$  over any 15cm aperture. The sample beam source point was adjusted for collimation using a wedge plate interferometer. The sample beam's perpendicular alignment to the test object's face was made using the turning mirrors' tip tilt adjustments and back-reflection. The test object image plane was locating at the MLA by reimaging an illuminated optical fiber tip placed at the mirror face. A polished reference strip mirror (35 x 0.5 cm  $< \lambda/2$  per cm) was inserted in the sample beam prior to the test object, located to obscure only a single row of sample zones, and made parallel to the test object face. This reference mirror was mounted from the stationary base of the LZS transit stage to help independently determine whether MLA foci motions are caused by deflections of the test apparatus, the vacuum chamber, or the test object. The test mirror was tip-tilt mounted including a precision dial gauge used to calibrate the LZS angular sensitivity. Figure 8 shows the measured MLA foci returned from the test mirror and reference flat.

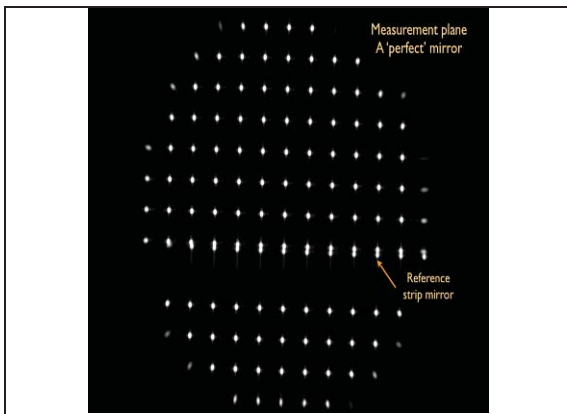


Figure 8 An array of foci returned from an LZS observation of a test flat mirror in vacuum. Each spot corresponds one of the 7.3mm sized contiguous zones that sample on the mirror. The foci for a reference strip mirror inserted in the view field are also seen.

The MLA foci image quality, stability, and slope sensitivity was examined upon chamber evacuation and operation. Chamber mechanical deflection upon evacuation was noted by the relative vertical deflection of the reference strip mirror foci compared to that from the test mirror (see Figure 8). The deflection is repeatable and found to be due to differential pressure seating the chamber door upon which the LZS instrument is mounted. The centroid of the foci were found to be stable to  $< 0.1$  pixel during

cryo pumping operations for camera integration times exceeding 100 msec. The test mirror was tilted by known increments and foci shift measured to yield the slope sensitivity and precision available with this test object. Using

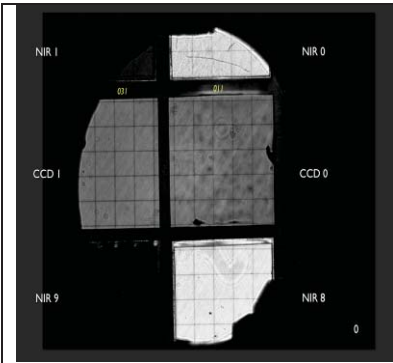


Figure 9 An image of the focal plane sensors (large grey and white regions) in one measurement field, along with the arrangement of microlens sample zones (thin grid).

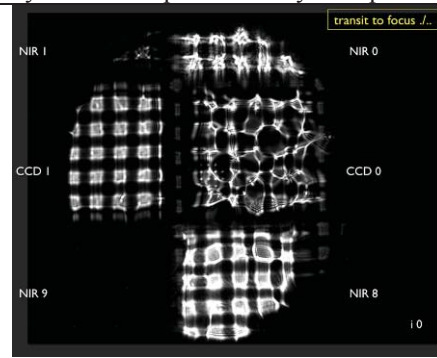


Figure 10 The Zone images distortion at mid-transit between the focal plane image and the micro lens focus measurement plane indicates local non-planarity on the sensors

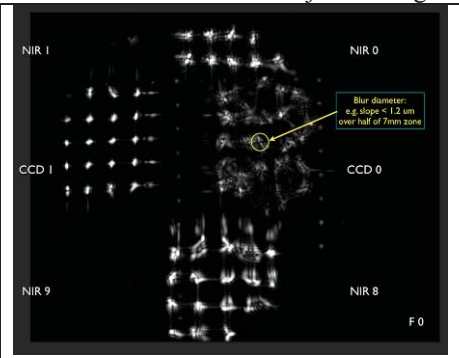


Figure 11 The focal quality at the micro lens focus measurement plane differs per sensor. The shape of the focal spot is a function of the distribution of surface slopes within a measurement zone.

Gaussian peak fitting, the formal centroiding error for the foci was found to be 0.02 pixels and the slope sensitivity to be 161 +/- 0.87 pixels/mrad. Scaling to slope measurement units, the slope measurement error,  $dm = 0.001 \mu\text{m}/\text{cm}$ , several orders of magnitude better than our requirements, albeit for a near perfect surface.

#### 4.2 Room temperature measurements of sensors on a 4x4 Demonstrator

The LZS system was used at room temperature to observe the JDEM Demonstrator that was half-populated (4x4) with a mix of CCD, near infrared (NIR), and unfinished NIR sensors with a read-out integrated circuit (ROIC) on the surface. This provided an opportunity to establish beam alignment with the focal plane and to witness the quality of data returned from the actual sensor surfaces that, in comparison to the test mirror, are both less perfectly planar and have much lower reflectivity. An image sample of the focal plane along with the arrangement of sample zones is shown in Figure 9. As the camera transits to the measurement plane (see Figure 10 and Figure 11), two phenomena are evident - first that the signal return from one sensor (CCD0) translates substantially with respect to the others, and second that the each sensor forms markedly different focal shapes. The global shift of CCD0's foci indicates that this sensor face has an overall tilt of  $\sim 75 \mu\text{m}$  along its width with respect to the others. The substantial non-planarity of the different sensors is also evidenced by the lack of signal from sensor NIR1 and NIR9, which are tipped at such significant angles that their reflected flux misses the pupil of the measurement system. Good flux returns from these sensors can be obtained by adjustment of the LZS beam turning mirror located outside of the vacuum chamber. The observations are consistent with

the fact that the sensors were not shimmed to be planar in this Demonstrator assembly. The final JDEM focal plane assembly plan includes shimming all sensors to be planar within a few microns.

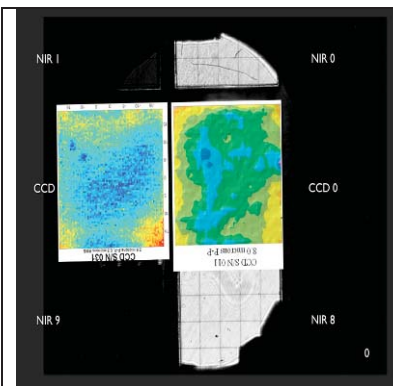


Figure 12 The measurement region shown in Figure 9, overlaid with color coded direct surface height measurement data of individual sensors at room temperature. Yellow is high and dark blue is low compared to the mid plane. The sensor to the right that has inherently high local slope that corresponds to the LZS foci size.

The distorted foci shapes are evidence that the surface topology of the different sensors varies substantially. For example, while the CCD1 zones converge to concise well-formed foci, the NIR sensor zones converge to irregular shaped foci, and the CCD0 zone foci are highly irregular (and the most irregular of the 16 sensors observed). The irregular foci do not resolve to well formed ones at other focal distances and indicate variations of surface slope *within* a sampled zone. For example, if we equate a constant slope within half a zone's width to the slope angle indicated by the typical radius of an irregular foci, then the corresponding height deviation is  $\sim 1 \mu\text{m}$ . We are able to confirm this interpretation by comparing the LZS results with direct displacement measurements of sensor height made on at room temperature. Figure 12 shows the focal plane image together with these direct data. Indeed the LZS spot shape and sizes correspond to local slope features and magnitudes on the sensor face. No direct measurements of the NIR sensors were yet available, so these data represent new information on

the inherent topology of these units. In fact, the distribution of angular slopes within a zone can be used derive from the Fourier transform of the zone's foci and, by recording images at different focal distances from the MLA, the absolute sense of zone curvature can also be derived. Such analysis is beyond the scope of our work at present.

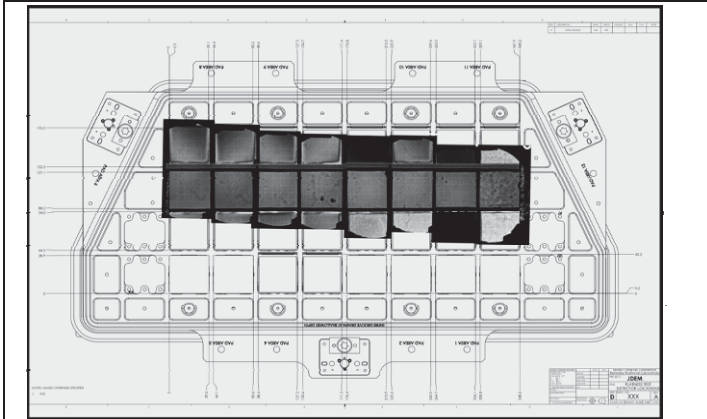


Figure 13 A composite image of the 4x8 focal plane sensors observed by the LZS system overlaid with a mechanical layout of the focal plane. The central observed stripe of sensors are CCD units. The other sensors are mixed HgCdTe and ROIC units. Then sensor columns are numbered from zero to size from right to left.

The LZS surface profile result depends on the ability to localize a zone's foci in the measurement plane and track the change in the foci's position. We tested our ability to locate the distorted foci obtained from the sensors. Using simple Gaussian fitting we find a formal centroid error of  $\sim 0.08$  pixels, which, given the slope sensitivity, corresponds to a slope measurement error of  $0.05 \mu\text{m}/\text{cm}$ , factors of several better than required.

In summary, our findings from the 4x4 Demonstrator LZS tests at room-temperature are that: direct sensor surface measurements correspond well to the LZS results, typical CCD sensors are more optically flat than NIR sensors with one notable exception, ROIC's sensors are similarly flat to the CCD's, and un-shimmed sensors are typically mounted with relative slopes of  $20\text{-}30 \mu\text{m}$  per sensor width.

### 4.3 Cryo-cycle measurements of the 4x8 Demonstrator

The LZS system was used to observe the fully populated JDEM Demonstrator focal plane<sup>6</sup> from room temperature to cryogenic conditions. A superposition of the observed focal plane region and the full mechanical layout of the focal plane is shown in Figure 13. Based on the 4x4 Demonstrator results described above, the central row of the observed region was populated with CCD's in order to be able to track fine LZS foci in the measurement plane. The measurement procedure, following an initial slope sensitivity calibration, was to center the sample beam field on a column of sensors and optimize the flux return from the covered sensors by adjustment of the beam turning mirror. The micro lens zone sample arrangement was adjusted to well sample the limited sensor view above and below the central field. A starting-point focal-plane image and measurement foci image were each taken and then a series of foci images were recorded as the focal plane cooled to 135K. The LZS field was then centered on the adjacent sensor column and the procedure repeated, this time warming to room temperature. The procedure was repeated until all sensor columns had been

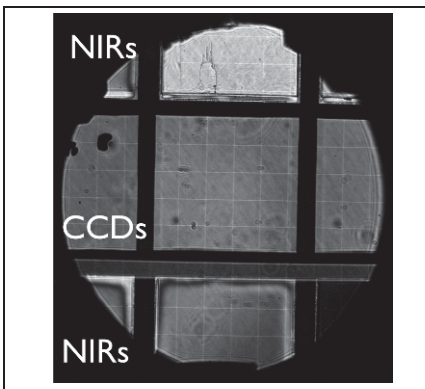


Figure 14 An image of the focal plane sensors (large grey and white regions) and the reference stripe mirror (grey horizontal region between CCD's and lower NIR's).

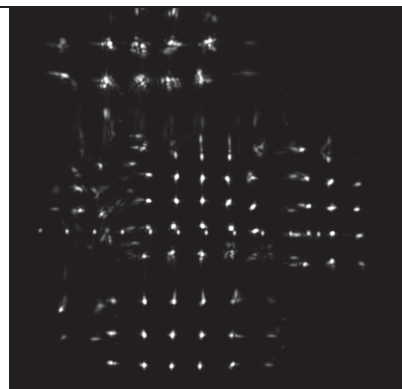


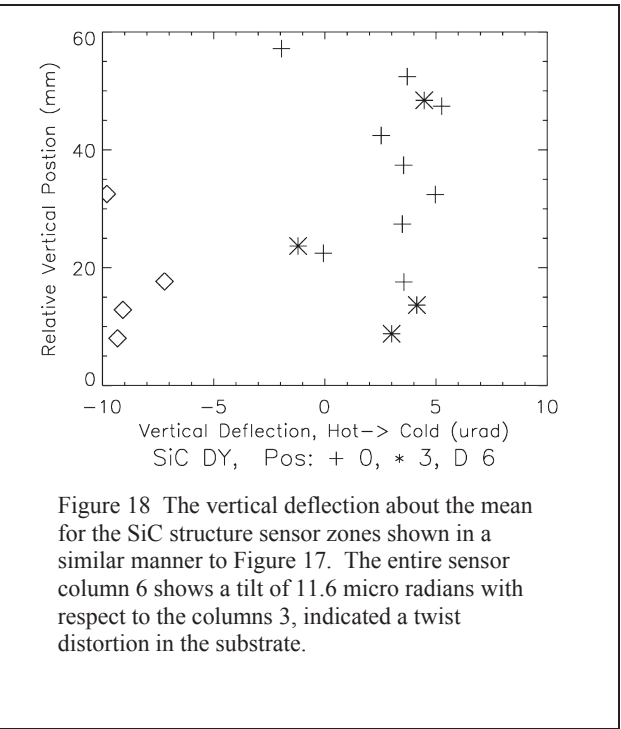
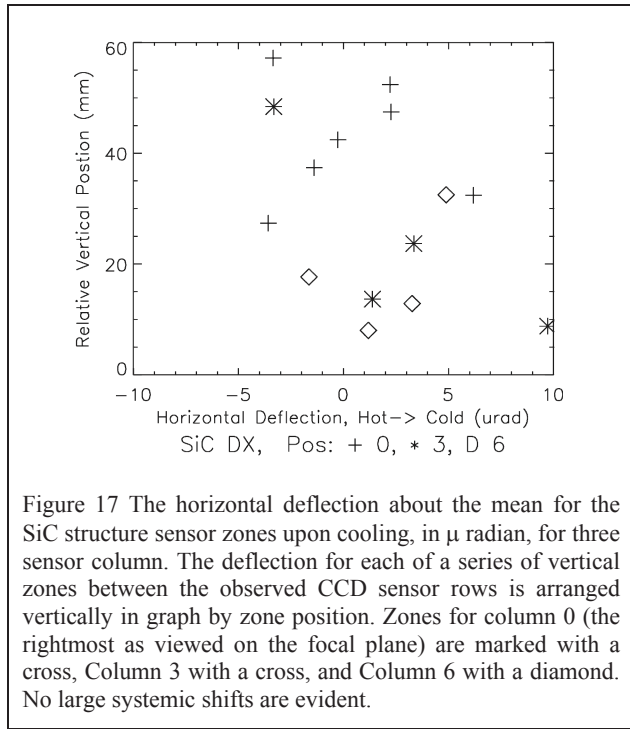
Figure 15 The measurement plane foci at 298K for the focal plane area of Figure 14. Foci shape for the top NIR and zones on sensor boundaries show local distortions.



Figure 16 The measurement plane foci at 135K for the focal plane area of Figure 14. The NIR and reference mirror foci are essentially unchanged while the CCD foci indicate significant local distortion.

measured. The test mirror calibration provides a slope measurement sensitivity of  $157.00 \pm 0.41$  pixel/mrad, a micro lens interval of  $74.27 \pm 0.14$  pixel, and an image scale of  $10.148 \pm 0.031$  pixel/mm, so that the zone sample size is 7.30 mm.

An image of the focal plane for one sample field, together with the arrangement of sample zones is shown in Figure 14. The room temperature and 135K foci returns for the field are shown in Figure 15 and Figure 16, respectively. The foci for the NIR sensors at the top and bottom of the field, as well as the reference strip mirror have remained essentially



intact while those for the CCD sensors have changed dramatically. This behavior is consistent for all of the sensor columns. Clearly the CCD sensors have undergone a substantial deformation. The CCD deformations, interpreted below, caused us to modify our measurement plan since we can only accurately follow zone foci from the NIR sensors above and below the CCD's. Further examination shows that small foci returns can be found from columnar regions *between* the sensors that correspond to reflections from the SiC focal plane structure itself. These foci offer an opportunity to independently track structure and sensor distortions. Data analysis shows that the NIR, reference mirror, and structure foci move in near unison, indicating that the entire focal plane has tipped nearly the same everywhere. It appears that that the flatness has been at most modestly affected by the cool-down because all of the zones have changed their slope by similar amounts.

The foci returns from the SiC structure were measured to obtain its deflection alone. The structure is visible in three narrow vertical regions between the CCD's, to the left of sensor columns 0, 3 and 6 (see Figure 13). The structure foci are well localized and their shape is stable with temperature. The horizontal and vertical deflection upon cooling for each of vertical region's zones is shown in Figure 17 and Figure 18, respectively. Following subtraction of the horizontal mean shift of  $-18.2 \mu\text{rad}$ , the column average horizontal shift magnitudes are  $< 3 \mu\text{rad}$  with RMS scatter in each column of  $\sim 5 \mu\text{rad}$ . By projecting the largest slope difference between any two adjacent columns, including the worst-case  $1-\sigma$  deviation, we estimate the maximum flatness deviation due to a linear slope across the 36 cm focal plane to be  $5.7 \mu\text{m}$ . In similar fashion, the column average vertical shift magnitudes are each  $2.7 \pm 2.6 \mu\text{rad}$  for columns 0 and 3, and  $-8.9 \pm 1.1 \mu\text{rad}$  for column 6 after removing the vertical mean shift of  $102 \mu\text{rad}$ . Therefore column 6 is significantly by a nearly uniform tilted by  $11.6 \mu\text{rad}$  with respect to the columns 0 and 3. Projecting this slope along the full 18 cm height of the focal plane results in an estimated flatness deviation of  $2.1 \mu\text{m}$  in the vertical direction.

The LZS foci for three zones on each NIR sensor were measured before and after cooling. The horizontal and vertical deflection upon cooling, averaged for each NIR sensor after subtracting the mean shift for all points, is shown in Figure 19 and Figure 20, respectively. The mean shift for all the foci that represents an overall tilt to the focal plane is  $-32.3 \mu\text{rad}$  and  $109 \mu\text{rad}$  in the horizontal and vertical directions, respectively, values that are quite similar in amplitude to that for the SiC structure alone. Therefore, to first order, the NIR sensor planes are following the structure. The LZS foci from the bottom of the upper NIR sensor and the top of the lower NIR sensor in each column move relatively in the horizontal direction by  $0.1 \pm 6.6 \mu\text{rad}$  and vertically toward each other by  $-34.1 \pm 7.2 \mu\text{rad}$ . We imply that the NIR

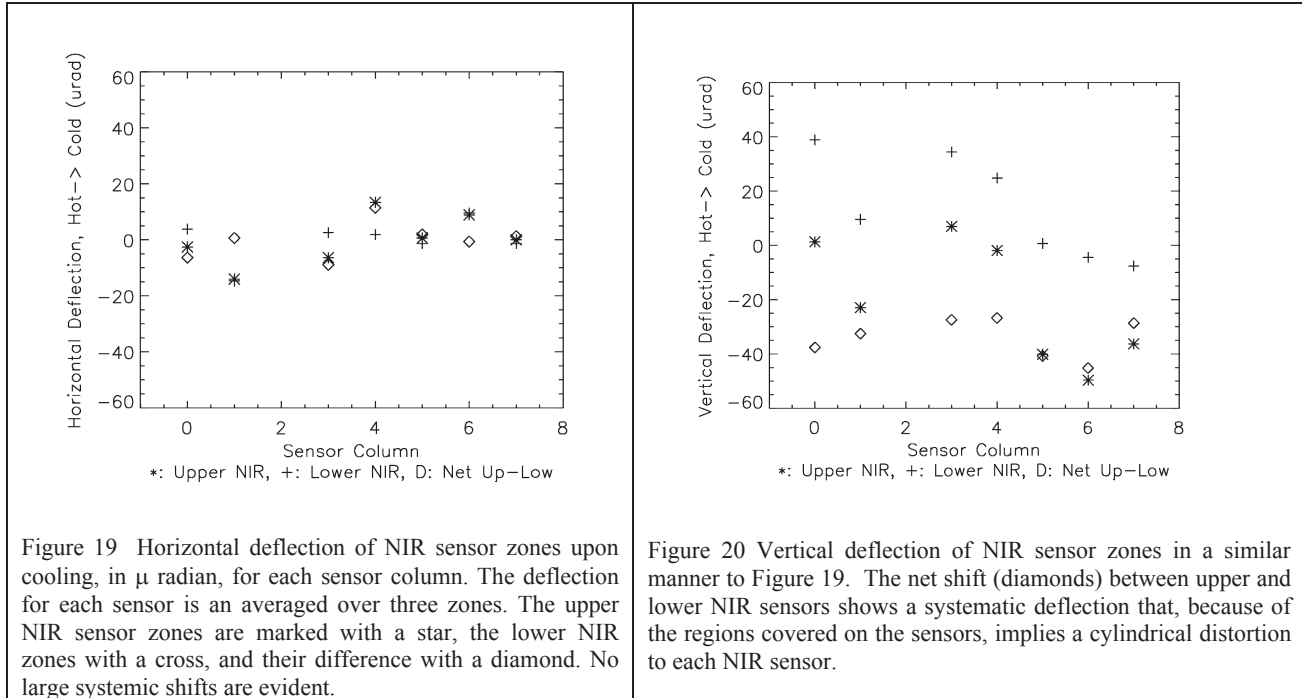


Figure 19 Horizontal deflection of NIR sensor zones upon cooling, in  $\mu$  radian, for each sensor column. The deflection for each sensor is an averaged over three zones. The upper NIR sensor zones are marked with a star, the lower NIR zones with a cross, and their difference with a diamond. No large systemic shifts are evident.

Figure 20 Vertical deflection of NIR sensor zones in a similar manner to Figure 19. The net shift (diamonds) between upper and lower NIR sensors shows a systematic deflection that, because of the regions covered on the sensors, implies a cylindrical distortion to each NIR sensor.

sensors are distorting into a cylindrical convex surface in the vertical dimension. Following this implication and scaling the relative slope differential between the upper and lower NIR regions to the height of the NIR sensor gives an estimated total linear flatness deviation of  $1.5 \mu\text{m}$  within the NIR sensor. We are unable to determine the actual shape of the NIR distortion from these data.

#### 4.4 Interpretation of the CCD sensor results

Time-lapse LZS data shows that all the CCD sensors are subject to a similar distortion upon cooling. Pronounced local slope changes for CCD's are evident in two stages of deformation. From 298K to  $\sim 240\text{K}$ , the left and right edges tilt up significantly, top and bottom edges tilt up less so, with some concavity forming in the middle of the detector. From  $\sim 240\text{K}$  to 135K, middle section grows significantly convex. We postulate the cause of distortion is differential thermal contraction between low CTE materials (Si, SiC) and higher CTE materials in the CCD package structure where an adhesive layer bonds the sensor surface to a supporting pedestal that includes a central opening for a flex circuit mounted electrical connector. We ran a finite element model in quarter section to predict the deflection shape. The model is run in two configurations because the adhesive layer material has different deformation stages about a glass transition at  $\sim 235\text{K}$ . Above this transition the material is rubbery (with an elastic modulus of  $E \sim 450\text{kPa}$ ) and inefficiently transmits shear while below 235K, the material becomes glassy and more rigid ( $E \sim 6000\text{kPa}$ ) and better shear transmitter. The modeled surfaces at 240K and 135K shown in Figure 21 and Figure 22 are consistent with the observed LZS data and indicate that the unsupported central section of the CCD sensor bows in a 'bi-metallic' effect. By estimating the slope from the cool down data of  $\sim 0.7\text{mrad}$  and scaling the modeled distortions by the ratio of measured slope change, we estimate that the maximum deflection of the CCD sensor surface is  $8.1 \mu\text{m}$  at 135K. We expect that future constructs of the CCD using a thicker Si substrate can have cryogenic deflection of a few microns. We anticipate improved LZS measurements of the local CCD distortions by using a micro lens with finer pitch and shorter focal length so that the returned foci stay well formed and translate within a more limited range on the recording camera.

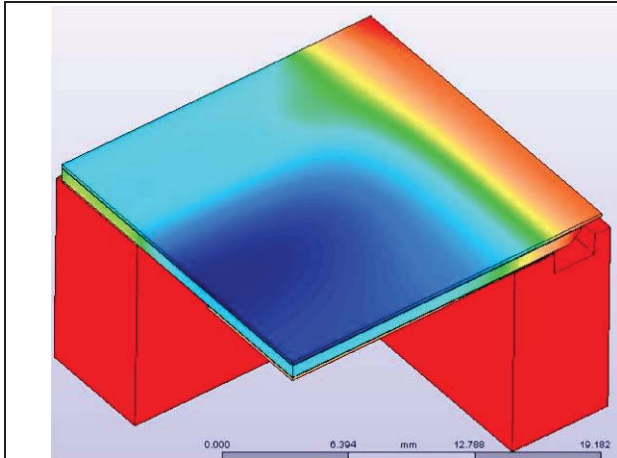


Figure 21 Modeled shape of one quarter of a CCD sensor assembly's surface at 240K with rubbery adhesive condition that poorly transmits shear between the substrate and the sensor surface. The Si CCD surface is a thin upper sheet adhesively bonded to a stiff SiC frame. Red and blue are positive and negative relative deflections in height, respectively.

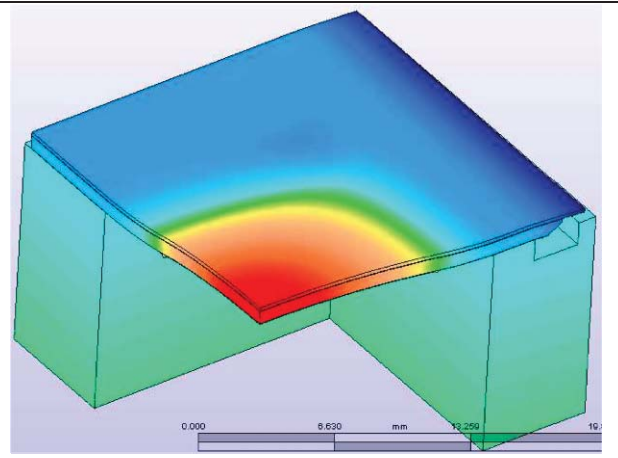


Figure 22 Modeled shape of one quarter of a CCD sensor assembly's surface at 135K with glassy adhesive condition that transmits shear more effectively than at higher temperatures.

## 5 CONCLUSION

A novel Local Zone Slope focal plane flatness measurement system has been developed to track changes in slope of the JDEM 4x8 Demonstrator focal plane surfaces undergoing cryogenic excursions. A deviation of flatness from the room-temperature configuration is inferred. Our results indicate deflections over the entire surface of the structure are less than  $\sim 5 \mu\text{m}$ . Flatness changes of the detector surfaces due to cooling are estimated to be  $\sim 1.5 \mu\text{m}$  for NIR detectors and less than  $8 \mu\text{m}$  for CCDs. We anticipate more informative LZS observations of the NIR, CCD, and focal plane cryo distortion will be obtained by using different slope sensitivity and zone samplings. The results can be enhanced by choosing micro lenses pitches and focal length, the sample beam magnification, and illumination masking.

## ACKNOWLEDGMENT

This work was supported by the Director, Office of Science, of the U.S. Department of Energy under Contract No. DE-AC02-05CH11231.

## REFERENCES

- <sup>1</sup> Sholl, M., et al, "Observatory Conceptual Development for the Joint Dark Energy Mission," Proc. SPIE 7436, 7436-03 (2009).
- <sup>2</sup> Aldering, G., et al., "Overview of the SuperNova/Acceleration Probe (SNAP)," Proc. SPIE 4835, 146-157 (2002).
- <sup>3</sup> Diehl, H.T., et al, "Characterization of DECam focal plane detectors," Proc. SPIE 7021, 7021-07 (2008).
- <sup>4</sup> Li, X., et al, "Surface Measurement with Shack-Hartmann wavefront sensing technology." Proc. SPIE, 7155 7155-15, (2008).
- <sup>5</sup> W.H. Southwell, "Wave-front estimation from wave-front slope measurements", J.Opt.Soc.Am.. Vol.70 (1980)
- <sup>6</sup> Besuner, R.W, "260 megapixel visible/NIR mixed technology focal plane for space", Proc. SPIE 8155A-12, San Diego (2011).